Anisotropic Ejecta Distribution of Kilonova AT 2017gfo

Zhi-Wei Shao,[1,2] Cheng-Jiang Yin,[1,2] Bin-Bin Zhang,[1,2,3] and Zi-Gao Dai[1,2]

[1]*School of Astronomy and Space Science, Nanjing University, Nanjing 210093, China*
[2]*Key Laboratory of Modern Astronomy and Astrophysics (Nanjing University), Ministry of Education, China*
[3]*Department of Physics and Astronomy, University of Nevada Las Vegas, NV 89154, USA*

ABSTRACT

Assuming that the ejecta produced during a binary neutron star merger is highly anisotropic, we propose an analytic model to fit the multi-wavelength data of AT 2017gfo, which is associated with the gravitational wave event GW170817. Our fitting results show that the observed data are consistent with the emission from a uniformly expanding ejecta with its mass and opacity anisotropically distributing with angle. The distribution of mass, velocity and opacity as functions of angle can be described by a cut-off power-law with different indices. The total mass of the ejecta is $M_{\text{total}} \simeq 0.081\ M_\odot$. The derived velocity of the ejecta is $v_{\text{ej}} \sim 0.27\ c$ and the opacity κ ranges from 4.2 cm^2 g^{-1} to 18 cm^2 g^{-1}, both being consistent with the results from the numerical simulations in previous works. Our results suggest that radiation from the polar region of ejecta dominates over that from the equatorial region at both early and late times due to the anisotropic structure and viewing angle effect. We also show that the relativistic Doppler effect and equal-arrival-time surface play an important role in shaping the observed kilonova light curve due to the high speed of ejecta.

Keywords: stars: neutron – gravitational waves

1. INTRODUCTION

Shortly after Hulse & Taylor (1975) discovered the first binary neutron star (BNS) system, considerable theories have pointed out that the merger of compact star binaries, neutron star-black hole (NS-BH), NS-NS (Lattimer & Schramm 1976; Symbalisty & Schramm 1982), can generate dynamical ejecta with enough high energy neutrons for heavy element ($A \gtrsim 140$) nucleosynthesis (*r-process*) (Metzger 2017, for review), completing the final puzzle of cosmic element origin. The rapid decay of the freshly synthesized lanthanide elements was later proposed to heat the BNS merger ejecta and produce a day-to-week luminous IR/optical/UV transient, which can be thousands of times brighter than novae, namely kilonova (KN) (Li & Paczyński 1998; Rosswog 2005; Metzger et al. 2010). Such kilonove are naturally expected to be associated with short gamma-ray bursts (sGRB). However, only some indirect evidence (Berger et al. 2005; Hjorth et al. 2005; Tanvir et al. 2013) was found during the past decades for such an association.

On August 17, 2017 at 12:41:04 UTC, the advanced LIGO/Virgo jointly detected a gravitational-wave event 40 Mpc away (Abbott et al. 2017b), which was later identified as a binary neutron star coalescence and named as GW170817. Merely 1.7 s after the trigger, an sGRB, GRB 170817A, was detected by both *Fermi* (Goldstein et al. 2017; Zhang et al. 2018) and *INTEGRAL* (Savchenko et al. 2017)

within the GW prediction area. About 11 hours after the trigger, several groups (first announced by Coulter et al. 2017) independently found an optical counterpart within the galaxy NGC 4993 and confirmed it to be a kilonova and named it as AT 2017gfo. The associated afterglow emission was later observed in X-ray and radio bands after several days (e.g. Troja et al. 2017; Hallinan et al. 2017). Such four phenomena, i.e., a gravitational wave event, a gamma-ray burst, a kilonova, and a multi-wavelength afterglow, which were observed in an NS-NS merger event, have marked the beginning of multi-messenger time domain astronomy era (see Abbott et al. 2017c, and references therein).

Both theoretical calculations and numerical simulations (Hotokezaka et al. 2013; Sekiguchi et al. 2015; Radice et al. 2018b) have suggested that a fraction of matter ($10^{-4} - 10^{-2}\ M_\odot$), known as dynamical ejecta, should be tidally disrupted and ejected with speed $v \sim 0.1 - 0.3\ c$ (c is the speed of light) in several milliseconds during the BNS merger. The dynamical ejecta is initially neutron-rich with an electron fraction $Y_e \sim 0.1 - 0.4$. The electron fraction at the polar region of the ejecta will then increase to $Y_e \gtrsim 0.3$ due to shock heating or weak interactions (Wanajo et al. 2014; Sekiguchi et al. 2015; Radice et al. 2016). Another source of ejecta originates in a neutrino-driven wind and viscosity-driven outflow (hereafter referred as a secular component) from the remnant accretion disk and generally propagates with speed $v \lesssim 0.1\ c$ (Perego et al. 2014; Siegel et al. 2014;
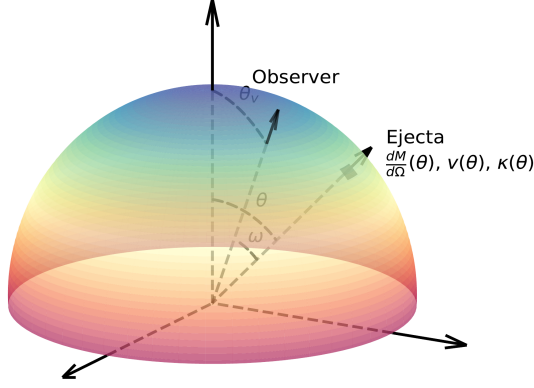
Figure 1. Schematic of our structured ejecta model. Colors represent the distribution of opacity κ from low (blue) to high (red). The viewing angle is θ_v and ω, ϕ (not marked) are the co-altitude and azimuth in the observer frame respectively.

Just et al. 2015; Martin et al. 2015; Wu et al. 2016; Fujibayashi et al. 2018). The evolution of KN ejecta thus leads to different regions with different Y_e. Previous works have shown that using the "red" ($Y_e \lesssim 0.3$, higher opacity and lanthanide-rich) and "blue" (higher Y_e and lanthanide-poor due to mild *r-process* nucleosynthesis) components can successfully explain the early IR/optical light curves (LC) and spectra (Cowperthwaite et al. 2017; Troja et al. 2017; Drout et al. 2017) of AT 2017gfo. In addition, it has been realized that a third intermediate "purple" component is required to explain the additional week-to-month multi-wavelength data (Villar et al. 2017). On the other hand, alternative approaches such as using a simplified semi-analytic anisotropic model of the ejecta (Perego et al. 2017) or carefully considering the radiative transfer via a two-dimensional numerical simulation (Kawaguchi et al. 2018) were attempted to relieve the apparent multi-component issue.

In this paper, we propose an anisotropic model with minimal physical assumptions and calculated resultant KN emission from the first principle. Similar to Huang et al. (2018), we take into account a smooth distribution of the ejecta mass per solid angle, velocity and opacity as functions of jet angle. We also consider the Doppler effect and equal-arrival-time surface (EATS) in detail. Our model is described in §2. The fitting procedure between our model and data is described in §3. The fitting results are then presented in §4, followed by discussions and conclusions in §5.

As illustrated in Figure 1, the ejecta distribution is modeled by a cutoff power law function[1],

$$F(\theta) = \begin{cases} F_0, & 0 < \theta \leqslant \theta_0, \\ F_0 \left(\frac{\theta}{\theta_0}\right)^{\delta_F}, & \theta_0 < \theta < \pi/2, \end{cases} \quad (1)$$

where $F = dM_{\rm ej}/d\Omega$ or $v_{\rm ej}$ or $\kappa_{\rm ej}$ or T_c stands for either the angular distribution of ejecta mass $dM_{\rm ej}/d\Omega$, velocity $v_{\rm ej}$, opacity $\kappa_{\rm ej}$ or temperature floor T_c. F reaches its extremum within θ_0, which can be regarded as a "blue" component in the polar region, whereas F changes as a power law when θ approaches $\pi/2$ which can be regarded as a "red" component in the equatorial region. As shown in §4, these continuous distributions can naturally lead to a smooth light curve without artificially introducing multiple components to explain the data.

According to Korobkin et al. (2012), the input radioactive energy rate is proportional to the *r-process* mass, so we have

$$\frac{dL_{\rm in}}{d\Omega}(t,\theta) = 4 \times 10^{18} \frac{dM_{\rm ej}}{d\Omega} \left[0.5 - \frac{1}{\pi}\arctan\left(\frac{t-t_0}{\sigma}\right)\right]^{1.3} {\rm erg\ s}^{-1},$$
(2)

where $t_0 = 1.3$ s and $\sigma = 0.11$ s are empirical constants. However, not all the radioactive energy could be converted to power KN. The cross section of the ejecta material to high energy γ−rays, neutrinos and particles created by decay process can introduce a thermalization efficiency $\epsilon_{\rm th}$. Barnes et al. (2016) provides an empirical equation:

$$\epsilon_{\rm th}(t,\theta) = 0.36\left[e^{-at} + \frac{\ln(1+2bt^d)}{2bt^d}\right], \quad (3)$$

where a, b, and d are constants related to the ejecta mass, velocity and the magnetic fields of the merger object and are listed as Table 1 in Barnes et al. (2016). We find that such a table can be successfully fitted by the following empirical function,

$$a, b = c_1 + c_2(v_{\rm ej} - c_3)\ e^{-(c_4 m_{\rm ej})^{0.2}}$$
$$d = c_1 + c_2 v_{\rm ej} + c_3 m_{\rm ej} \quad (4)$$

where c_i are free parameters, which are listed for a, b and d in Table 1. We note that $m_{\rm ej}$ in Eq.3 and Eq.4 is the total mass within a homologous photosphere while the ejecta mass in our model represents the angular density per solid angle. Thus, a factor of 4π should be multiplied to obtain the equivalent spherical mass when calculating the efficiency in Eq.3.

After obtaining the input energy and thermal efficiency, the bolometric luminosity can be calculated following Arnett

2. THE KILONOVA MODEL

---

[1] We have also investigated other distributions such as $F(\theta) = \exp(\alpha\theta^2)$ and $F(\theta) = (1 + \theta/\theta_0)^{\delta_F}$, while both were disfavored by fitting results.

Table 1. a, b, d FITTING PARAMETERS

	c_1	c_2	c_3	c_4
a	0.292	3.76×10^2	5.27×10^{-2}	9.67×10^4
b	0.121	92.3	7.16×10^{-2}	2.52×10^5
d	0.724	7.57	2.55	-

(1980, 1982) and Chatzopoulos et al. (2012):

$$\frac{dL_{\text{bol}}}{d\Omega} = e^{-(t/t_d)^2} \int_0^t \frac{dL_{\text{in}}}{d\Omega} \epsilon_{\text{th}} \, e^{(t'/t_d)^2} \frac{2t'}{t_d^2} dt', \qquad (5)$$

where $t_d = \sqrt{2\kappa m_{\text{ej}}/\beta v c}$ is the geometric mean diffusion timescale with general density profile constant $\beta = 13.8$. The radiation can be approximately described by a blackbody spectrum with effective temperature T,

$$\frac{dL_{\text{bol}}}{d\Omega}(t,\theta) = (v_{\text{ej}}t)^2 \sigma_{\text{SB}} T^4(t,\theta). \qquad (6)$$

Numerical simulations (Barnes & Kasen 2013) indicate that a critical temperature exists at which the ejecta temperature stops further decrease. This can be related to the lanthanide abundance and their first ionization temperature. Hence we assume this temperature floor also complies with Eq.1 distribution and the photosphere temperature can be written as

$$T_{\text{phot}}(t,\theta) = \begin{cases} T(t,\theta), & T \leqslant T_c, \\ T_c(\theta), & T > T_c. \end{cases} \qquad (7)$$

The exact photosphere radius is derived accordingly by

$$R_{\text{phot}}(t,\theta) = \begin{cases} v_{\text{ej}}t, & T \leqslant T_c, \\ \left(\frac{T}{T_c}\right)^2 v_{\text{ej}}t, & T > T_c. \end{cases} \qquad (8)$$

As shown in Figure 1, the polar angle in the source frame θ can be rewritten as a function of the co-altitude ω and azimuth ϕ in the observer frame, which is used in further calculations,

$$\theta(\phi,\omega) = \arccos\left(\cos\theta_v \cos\omega - \sin\theta_v \sin\omega \cos\phi\right). \qquad (9)$$

As the ejecta velocity ($\sim 0.3\,c$, Villar et al. 2017; Perego et al. 2017) reaches the sub-relativistic regime, the Doppler effect should be taken into account to calculate the observed energy flux. Following Eq.(4.110) in Rybicki & Lightman (2008), we have

$$\frac{I(\nu_o)}{\nu_o^3} = \frac{B(\nu_s,T)}{\nu_s^3}, \qquad (10)$$

where ν_o is the frequency corresponding to the central wavelength of a given band in the observer frame, ν_s is the emitted frequency in the ejecta frame, and $B(\nu,T)$ is the Planck function, i.e.,

$$B(\nu,T) = \frac{2h\nu^3}{c^2} \frac{1}{e^{h\nu/kT} - 1}.$$

The observed frequency is

$$\nu_o = \frac{\nu_s}{\Gamma(1 - \beta\cos\omega)}, \qquad (11)$$

where $\beta = v_{\text{ej}}(\theta)/c$, $\Gamma = 1/\sqrt{1-\beta^2}$ and ω is introduced in Eq.9. Thus $\nu_s = \Gamma(1-\beta\cos\omega)\nu_o$ is a function of (θ,ω) and we could get the observed intensity $I(\nu_o)$ in each band.

Finally, similar to Eq.4&5 in Martin et al. (2015), we obtain the observed flux density by integrating over the EATS of the ejecta that is moving towards the observer,

$$\begin{aligned} \mathcal{F}(\nu_o,t_o) &= \iint\limits_{\text{semisphere}} I(\nu_o) \frac{R_{\text{phot}}^2(t',\theta)}{D_L^2} \cos\omega \, d\Omega' \\ &= \frac{\nu_o^3}{D_L^2} \iint\limits_{\text{semisphere}} B\left(\nu_s(\theta,\omega), T_{\text{phot}}(t',\theta)\right) \frac{R_{\text{phot}}^2(t',\theta)\cos\omega}{\nu_s^3(\theta,\omega)} d\Omega', \end{aligned} \qquad (12)$$

where t' is a function of (θ,ω,t_o) given by EATS, and D_L is the distance to the source and we adopt $D_L = 43.8$ Mpc, according to Abbott et al. (2017a).

3. DATA AND FIT

3.1. *The Unified Dataset*

The multi-wavelength light curve data are taken from Table 3 in Villar et al. (2017) and the open kilonova catalog[2]. The data set is a collection of observations originally presented in Andreoni et al. (2017); Arcavi et al. (2017); Coulter et al. (2017); Cowperthwaite et al. (2017); Díaz et al. (2017); Drout et al. (2017); Evans et al. (2017); Hu et al. (2017); Valenti et al. (2017); Kasliwal et al. (2017); Lipunov et al. (2017); Pian et al. (2017); Pozanenko et al. (2018); Shappee et al. (2017); Smartt et al. (2017); Tanvir et al. (2017); Troja et al. (2017); Utsumi et al. (2017), with all upper limits and W band data excluded. For simplicity, we only take the data measured in AB magnitude. Upper limits and unfiltered data are not taken into account. Extinction caused by the Milky Way was corrected following Fitzpatrick (1999).

3.2. *Fitting Procedure*

Our model (Eq.12) is then fitted to the observational data using a Markov Chain Monte Carlo approach. A Python package, emcee (Foreman-Mackey et al. 2013), is utilized for sampling and getting posterior predictions on our model parameters.

---

[2] http://kilonova.space/

Table 2. BEST FIT PARAMETERS

$\log m_0$ $(M_\odot)$	v_0 (c)	$\log \kappa_0$ $(\mathrm{cm^2\ g^{-1}})$	$\log T_c$ (K)	δ_m	$\log(-\delta_v)$	δ_κ	δ_T	σ	θ_0 $(°)$	χ^2/dof[a]
$-2.836^{+0.012}_{-0.012}$	$0.276^{+0.007}_{-0.007}$	$0.626^{+0.046}_{-0.048}$	$3.582^{+0.010}_{-0.010}$	$8.387^{+0.779}_{-0.695}$	$-3.585^{+1.604}_{-1.635}$	$3.835^{+0.339}_{-0.329}$	$-7.671^{+1.438}_{-2.209}$	$0.268^{+0.010}_{-0.010}$	$61.511^{+1.516}_{-1.538}$	1.024

[a]Calculated with the σ term in Eq.13.

The log-likelihood function is defined as

$$\ln \mathcal{L} = -\frac{1}{2} \sum_{i=1}^{n} \left[\frac{(O_i - M_i)^2}{\sigma_i^2 + \sigma^2} + \ln \left(2\pi(\sigma_i^2 + \sigma^2)\right) \right], \quad (13)$$

where n is the total number of observation points (in our case, $n = 557$), O_i, M_i, σ_i are the ith observed magnitude, modeled magnitude and observed uncertainty. We also introduce a scatter term, σ, to account for any additional systematic error. σ is treated as a free parameter during the fit.

There are ten free parameters in our model, namely, (1) m_0, initial (polar region) value of ejecta mass per solid angle, (2) v_0, ejecta velocity at polar region, (3) κ_0, opacity at polar region, (4) T_c, temperature floor at polar region, (5) δ_m, power law index of mass distribution, (6) δ_v, power law index of velocity distribution, (7) δ_κ, power law index of opacity distribution, (8) δ_T, power law index of temperature distribution, (9) θ_0, critical angle, and (10) σ, systematic error term.

The priors of m_0, κ_0, T_c and δ_v are set to be log-uniform because they may spread several orders of magnitude with changing power-law indices and critical angle[3]. The other parameters are all set with flat priors. The viewing angle is fixed to $\theta_v = 30°$ (Abbott et al. 2017b; Hajela et al. 2019).

We then run *emcmc* for $n_{\rm walkers} \times n_{\rm steps} = 100 \times 11600$. To check the convergence of our chains, we follow the `emcee` documentation[4] and perform an autocorrelation analysis. The estimated integrated autocorrelation time τ_f is less than 230 for all 10 parameters, meaning this can be considered as a reliable estimation because $n_{\rm steps}/\tau_f > 50$. Thus we could safely discard the first 4000 steps, treating them as burn-in phase.

4. RESULTS

The best-fit model is over-plotted with the observed data in Figure 2. Constraints on parameters are shown in Table 2 and Figure 3. In Figure 4 we plot the angular distributions of ejecta mass, velocity, opacity and temperature of our best-fit model.

Based on our results, we get the total mass of the ejecta $M_{\rm total} \simeq 0.081\ M_\odot$ by integrating over the sphere. In order

to compare with previous researches (e.g., Villar et al. 2017), we also define a "blue" region (or the polar region) of which ejecta polar angle $\theta \leq \theta_0$ and a "red" region (or the equatorial region) for the ejecta with the polar angle $\theta_0 < \theta \leq 90°$. And the mass of the blue region is $M_{\rm blue} \sim 0.010\ M_\odot$. The high ejecta velocity $v_{\rm ej} = 0.276\ c$ and its corresponding power-law index $\log(-\delta_v) = -3.835$ indicate a flat velocity distribution, as shown in Figure 4. The opacity $\kappa_{\rm ej}$ ranges from $\sim 4.2\ \mathrm{cm^2\ g^{-1}}$ at the polar region to $\sim 18\ \mathrm{cm^2\ g^{-1}}$ at the equatorial plane. And the temperature floor T_c decreases from ~ 3800 K to ~ 200 K as θ increases. During the time interval we investigated ($t \lesssim 26$ day), the ejecta within $\theta \lesssim 80°$ has cooled to its corresponding temperature floor ($T_c \approx 550$ K at $\theta \approx 80°$). As polar angle further increases, the actual temperature begins to rise and reaches $T \approx 800$ K at $\theta = 90°$.

In Figure 5 we compare our model-predicted spectral energy distribution (SED) with the observed data at different times, which again shows our modeling successfully reproduced the spectral evolution of the kilonova emission.

To compare our results with Villar et al. (2017), we plot the calculated blue and red component of our model of each individual band in Figure 6. The blue curves represent the emission from the polar region, red curves from the equatorial region and black curves are the sum of these two components. Our results are consistent with Villar et al. (2017) in terms of the peak time of the blue and red components. However, our results show that the blue component still dominates the emission at a late time, likely due to the introudced anisotropic structure of the ejecta. This can be seen in Figure 1, where an observer at $\theta_v = 30°$ will naturally receive more radiation from polar region. The equatorial component will dominate at late time only when the viewing angle is large enough (e.g., $\theta_v = 90°$). Additionally, the distribution of T_c in our model is different. The blue component in our model has higher temperature floor, while in Villar et al. (2017) T_c of red & purple components are higher. T_c is a factor that "controls" the allocation of energy into different bands for a given $L_{\rm bol}$ determined in Eq.5, which can lead the light curves to behave differently.

5. DISCUSSIONS & SUMMARY

We have successfully modeled the multiwavelength light curves of the kilonova AT 2017gfo by utilizing an anisotropic ejecta distribution of the ejecta and yield the following main

---

[3] During the fitting process, we firstly limit δ_v to be negative and use a flat prior. While the results show $\delta_v \approx 0$, so we use a log-uniform prior (i.e., a flat $\log(-\delta_v)$) instead to better investigate its distribution.

[4] https://emcee.readthedocs.io/en/latest/tutorials/autocorr/

conclusions: (1) we find a cutoff power law model in the ejecta structure fits best to the observed data. (2) Our best-fitting model leads to a uniformly expanding photosphere with $M_{\text{total}} \simeq 0.081\,M_\odot$ (among which $\sim 0.010\,M_\odot$ from polar region and the else from equatorial region), $v_{\text{ej}} \sim 0.27\,c$ and opacity $4.2\,\text{cm}^2\,\text{g}^{-1} \lesssim \kappa_{\text{ej}} \lesssim 18\,\text{cm}^2\,\text{g}^{-1}$. (3) Our modeling coincides with dynamical ejecta moving at $v \approx 0.2 - 0.3\,c$, in which case the relativistic Doppler effect and EATS play an important role in shaping the observed light curve. (4) We find although the mass of the polar region is only a small fraction of the total mass, emission from the polar region dominates at later time for most bands, which is mainly caused by the anisotropic structure when viewed from the polar direction and the influence of a different T_c distribution which is higher at the polar region.

We have noticed that the total ejecta mass in our model $M_{\text{total}} \simeq 0.081\,M_\odot$, although consistent with some of the previous results (Villar et al. 2017; Perego et al. 2017) in general, is still significantly higher than the mass of the dynamical and secular components predicted in a series of recent numerical simulations (e.g., Hotokezaka et al. 2013; Martin et al. 2015; Fujibayashi et al. 2018; Radice et al. 2018b). Our results thus suggest that additional central power from the central engine is needed. Possible sources of such power include the nebular wind (Ren et al. 2019) and hybrid energy input by a long-lived remnant (Yu et al. 2018; Li et al. 2018). The central engine could be further constrained with the help of afterglows in future events (Xiao et al. 2017; Liu et al. 2020). Furthermore, the ejecta mass in our results is also subject to some ignorance of the physical details such as the direction preference of photon diffusion (Kawaguchi et al. 2018) in realistic radiation transfer calculations and that the coefficient in Eq.2 may change under different conditions (see Perego et al. 2017 and references therein). Those aspects have not been taken into account due to the limited scope of this study.

The uniform distribution of the high velocity in our results is consistent with the property of a dynamical ejecta in previous studies (Sekiguchi et al. 2015; Radice et al. 2018b). The higher dynamical ejecta mass in our results suggests additional components such as secular and viscous-dynamical components (Perego et al. 2017; Radice et al. 2018a; Fujibayashi et al. 2018) should be considered in future work. The best-fit of the opacity for the blue component is slightly higher than what was previously thought (Tanaka et al. 2018) but still consistent with a recent case study (Tanaka et al. 2019).
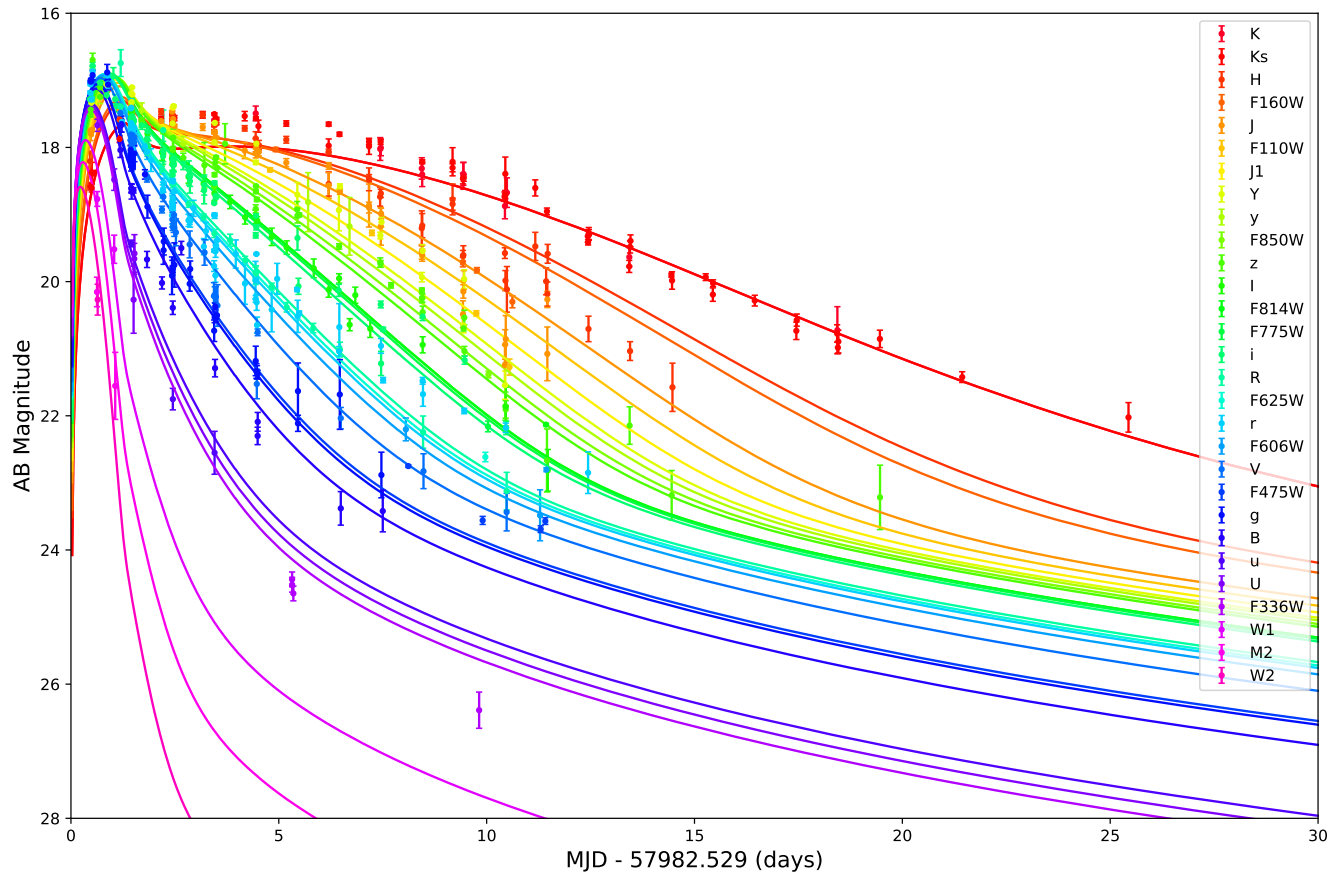
Figure 2. Multiwavelength observations of AT 2017gfo accompanied with our best-fit model. The magnitude values have already been corrected for extinction. *K* band and K_s band data are treated with the same central wavelength.
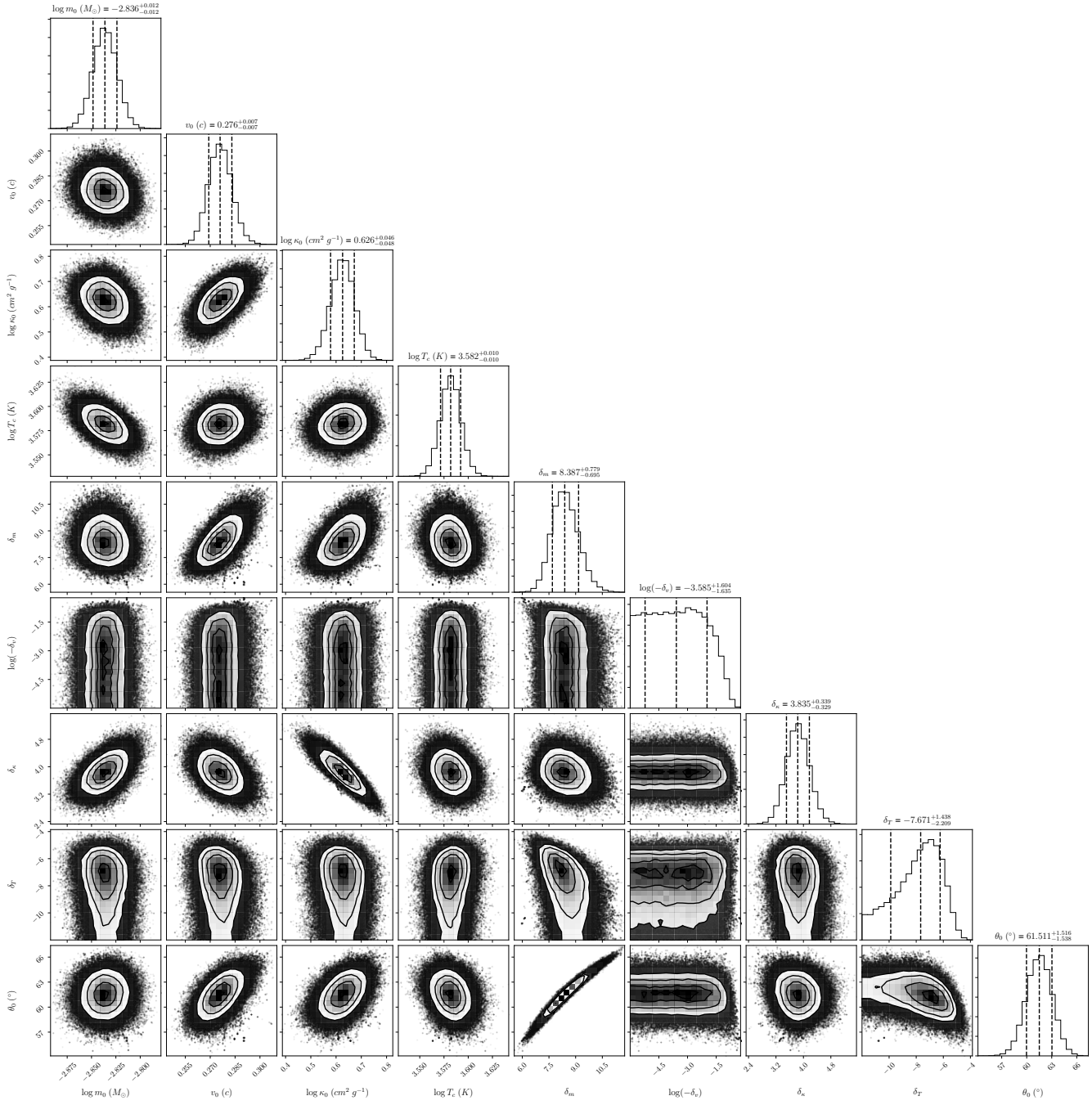
Figure 3. Corner plot illustrating posterior probability of our model. The strong correlation between θ_0 and δ_m is a natural result because both of them could control the changing slope of mass distribution. The flat distribution of $\log(-\delta_v)$ provides a rough lower limit $\delta_v \gtrsim -10^{-2}$.
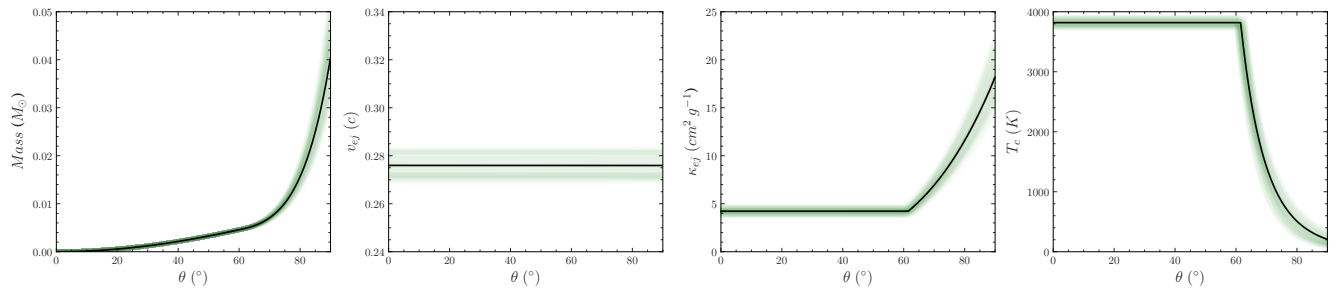
Figure 4. Distributions of ejecta physical properties as a function of polar angle θ. Panels from left to right are integrated mass (only semisphere, $\times 2$ to get the total mass), velocity, opacity and temperature floor. Black lines are the best-fitting model and green shades depict the 1σ uncertainties.
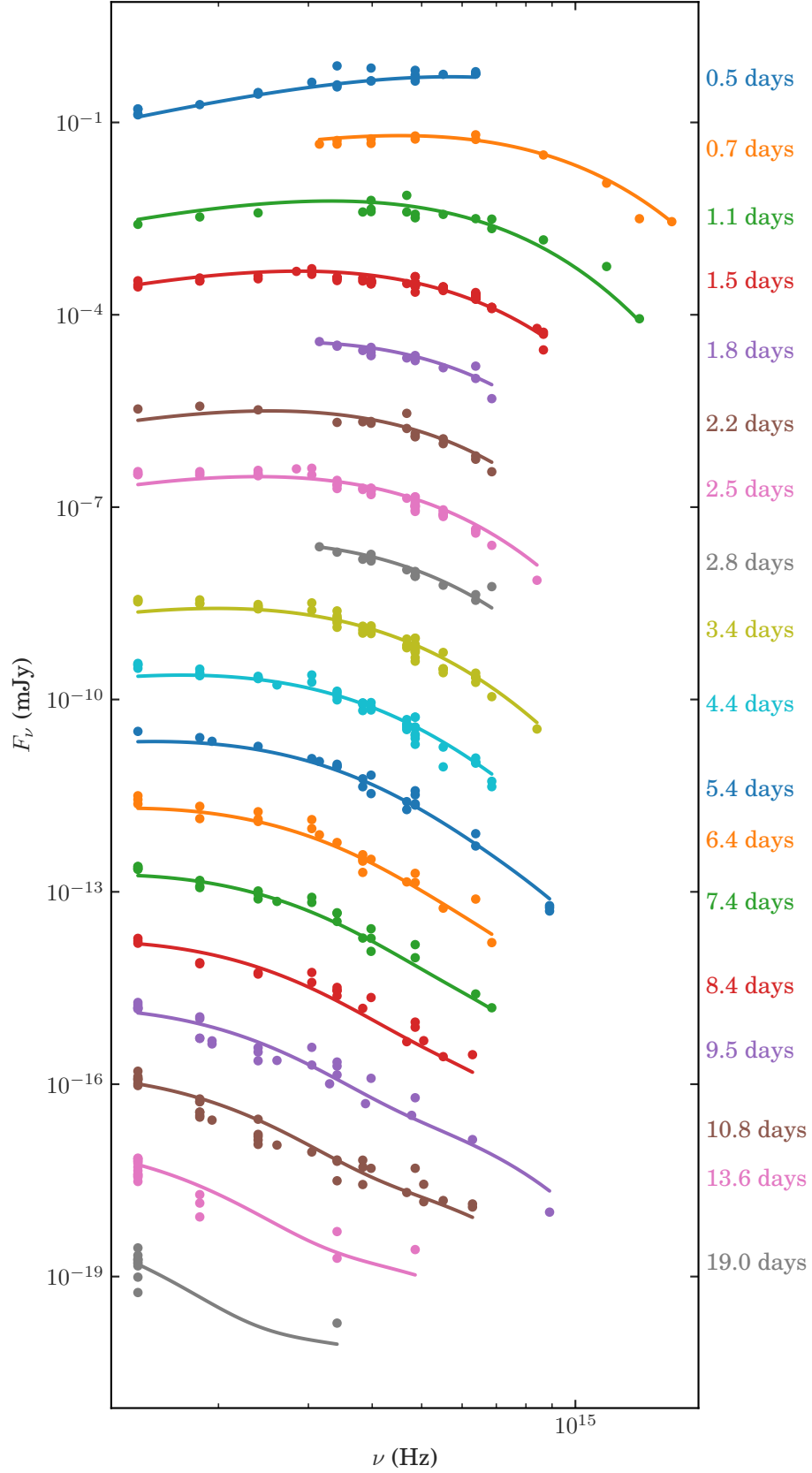
Figure 5. Time evolution of observed SED and our model results. The data are categorized via *K-means* clustering. Each curve is shifted down by 0.1 dex compared with the previous curve.
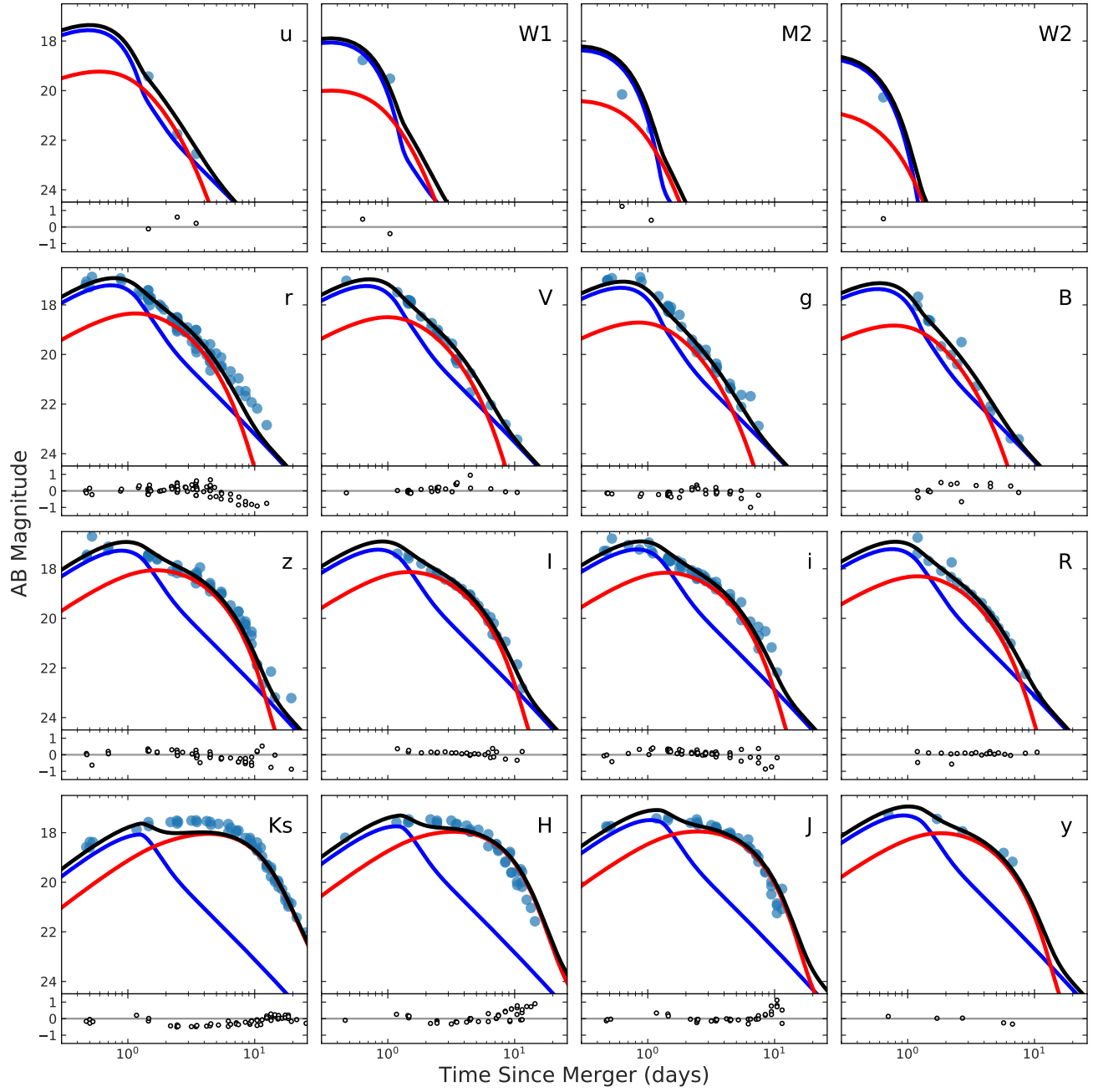
Figure 6. Observed and modeled LC in selected bands. Blue lines represent emission from polar region, red lines from equatorial region and black lines are the sum of of these two components. Observed magnitudes are shown in blue dots. The bottom panel of each subplot shows the residual.

REFERENCES

Abbott, B. P., Abbott, R., Abbott, T. D., et al. 2017a, Nature, 551, 85

—. 2017b, PhRvL, 119, 161101

—. 2017c, ApJL, 848, L12

Andreoni, I., Ackley, K., Cooke, J., et al. 2017, PASA, 34, e069

Arcavi, I., Hosseinzadeh, G., Howell, D. A., et al. 2017, Nature, 551, 64

Arnett, W. D. 1980, ApJ, 237, 541

—. 1982, ApJ, 253, 785

Barnes, J., & Kasen, D. 2013, ApJ, 775, 18

Barnes, J., Kasen, D., Wu, M.-R., & Martínez-Pinedo, G. 2016, ApJ, 829, 110

Berger, E., Price, P. A., Cenko, S. B., et al. 2005, Nature, 438, 988

Chatzopoulos, E., Wheeler, J. C., & Vinko, J. 2012, ApJ, 746, 121

Coulter, D. A., Foley, R. J., Kilpatrick, C. D., et al. 2017, Science, 358, 1556

Cowperthwaite, P. S., Berger, E., Villar, V. A., et al. 2017, ApJL, 848, L17

Díaz, M. C., Macri, L. M., Garcia Lambas, D., et al. 2017, ApJL, 848, L29

Drout, M. R., Piro, A. L., Shappee, B. J., et al. 2017, Science, 358, 1570

Evans, P. A., Cenko, S. B., Kennea, J. A., et al. 2017, Science, 358, 1565

Fitzpatrick, E. L. 1999, PASP, 111, 63

Foreman-Mackey, D., Hogg, D. W., Lang, D., & Goodman, J. 2013, PASP, 125, 306

Fujibayashi, S., Kiuchi, K., Nishimura, N., Sekiguchi, Y., & Shibata, M. 2018, ApJ, 860, 64

Goldstein, A., Veres, P., Burns, E., et al. 2017, ApJL, 848, L14

Hajela, A., Margutti, R., Alexander, K. D., et al. 2019, ApJL, 886, L17

Hallinan, G., Corsi, A., Mooley, K. P., et al. 2017, Science, 358, 1579

Hjorth, J., Watson, D., Fynbo, J. P. U., et al. 2005, Nature, 437, 859

Hotokezaka, K., Kiuchi, K., Kyutoku, K., et al. 2013, PhRvD, 87, 024001

Hu, L., Wu, X., Andreoni, I., et al. 2017, Science Bulletin, 62, 1433

Huang, Z.-Q., Liu, L.-D., Wang, X.-Y., & Dai, Z.-G. 2018, ApJ, 867, 6

Hulse, R. A., & Taylor, J. H. 1975, ApJL, 195, L51

Just, O., Bauswein, A., Ardevol Pulpillo, R., Goriely, S., & Janka, H. T. 2015, MNRAS, 448, 541

Kasliwal, M. M., Nakar, E., Singer, L. P., et al. 2017, Science, 358, 1559

Kawaguchi, K., Shibata, M., & Tanaka, M. 2018, ApJL, 865, L21

Korobkin, O., Rosswog, S., Arcones, A., & Winteler, C. 2012, MNRAS, 426, 1940

Lattimer, J. M., & Schramm, D. N. 1976, ApJ, 210, 549

Li, L.-X., & Paczyński, B. 1998, ApJL, 507, L59

Li, S.-Z., Liu, L.-D., Yu, Y.-W., & Zhang, B. 2018, ApJL, 861, L12

Lipunov, V. M., Gorbovskoy, E., Kornilov, V. G., et al. 2017, ApJL, 850, L1

Liu, L.-D., Gao, H., & Zhang, B. 2020, ApJ, 890, 102

Martin, D., Perego, A., Arcones, A., et al. 2015, ApJ, 813, 2

Metzger, B. D. 2017, Living Reviews in Relativity, 20, 3

Metzger, B. D., Martínez-Pinedo, G., Darbha, S., et al. 2010, MNRAS, 406, 2650

Perego, A., Radice, D., & Bernuzzi, S. 2017, ApJL, 850, L37

Perego, A., Rosswog, S., Cabezón, R. M., et al. 2014, MNRAS, 443, 3134

Pian, E., D'Avanzo, P., Benetti, S., et al. 2017, Nature, 551, 67

Pozanenko, A. S., Barkov, M. V., Minaev, P. Y., et al. 2018, ApJ, 852, L30

Radice, D., Galeazzi, F., Lippuner, J., et al. 2016, MNRAS, 460, 3255

Radice, D., Perego, A., Hotokezaka, K., et al. 2018a, ApJL, 869, L35

—. 2018b, ApJ, 869, 130

Ren, J., Lin, D.-B., Zhang, L.-L., et al. 2019, ApJ, 885, 60

Rosswog, S. 2005, ApJ, 634, 1202

Rybicki, G. B., & Lightman, A. P. 2008, Radiative processes in astrophysics (John Wiley & Sons)

Savchenko, V., Ferrigno, C., Kuulkers, E., et al. 2017, ApJL, 848, L15

Sekiguchi, Y., Kiuchi, K., Kyutoku, K., & Shibata, M. 2015, PhRvD, 91, 064059

Shappee, B. J., Simon, J. D., Drout, M. R., et al. 2017, Science, 358, 1574

Siegel, D. M., Ciolfi, R., & Rezzolla, L. 2014, ApJL, 785, L6

Smartt, S. J., Chen, T.-W., Jerkstrand, A., et al. 2017, Nature, 551, 75

Symbalisty, E., & Schramm, D. N. 1982, Astrophys. Lett., 22, 143

Tanaka, M., Kato, D., Gaigalas, G., & Kawaguchi, K. 2019, arXiv e-prints, arXiv:1906.08914

Tanaka, M., Kato, D., Gaigalas, G., et al. 2018, ApJ, 852, 109

Tanvir, N. R., Levan, A. J., Fruchter, A. S., et al. 2013, Nature, 500, 547

Tanvir, N. R., Levan, A. J., González-Fernández, C., et al. 2017, ApJL, 848, L27

Troja, E., Piro, L., van Eerten, H., et al. 2017, Nature, 551, 71

Utsumi, Y., Tanaka, M., Tominaga, N., et al. 2017, PASJ, 69, 101

Valenti, S., Sand, D. J., Yang, S., et al. 2017, ApJL, 848, L24

Villar, V. A., Guillochon, J., Berger, E., et al. 2017, ApJL, 851, L21

Wanajo, S., Sekiguchi, Y., Nishimura, N., et al. 2014, ApJL, 789, L39

Wu, M.-R., Fernández, R., Martínez-Pinedo, G., & Metzger, B. D. 2016, MNRAS, 463, 2323

Xiao, D., Liu, L.-D., Dai, Z.-G., & Wu, X.-F. 2017, ApJL, 850, L41

Yu, Y.-W., Liu, L.-D., & Dai, Z.-G. 2018, ApJ, 861, 114

Zhang, B. B., Zhang, B., Sun, H., et al. 2018, Nature
    Communications, 9, 447